Unraveling the potential and pore-size dependent capacitance of slit-shaped graphitic carbon pores in aqueous electrolytes

R. K. Kalluri,[†a] M. M. Biener,[†b] M. E. Suss,[bc] M. D. Merrill,[b] M. Stadermann,[b] J. G. Santiago,[c] T. F. Baumann,[b] J. Biener*[b] and A. Striolo*[a]

Understanding and leveraging physicochemical processes at the pore scale are believed to be essential to future performance improvements of supercapacitors and capacitive desalination (CD) cells. Here, we report on a combination of electrochemical experiments and fully atomistic simulations to study the effect of pore size and surface charge density on the capacitance of graphitic nanoporous carbon electrodes. Specifically, we used cyclic voltammetry (CV) and electrochemical impedance spectroscopy (EIS) to study the effect of potential and pore size on the capacitance of nanoporous carbon foams. Molecular dynamics simulations were performed to study the pore-size dependent accumulation of aqueous electrolytes in slit-shaped graphitic carbon pores of different widths (0.65 to 1.6 nm). Experimentally, we observe a pronounced increase of the capacitance of sub-nm pores as the applied potential window gets wider, from a few F g^{-1} for narrow potential ranges (-0.3 to 0.3 V *vs.* Ag/AgCl) to ~ 40 F g^{-1} for wider potential windows (-0.9 V to 0.9 V *vs.* Ag/AgCl). By contrast, the capacitance of wider pores does not depend significantly on the applied potential window. Molecular dynamics simulations confirm that the penetration of ions into pores becomes more difficult with decreasing pore width and increasing strength of the hydration shell. Consistent with our experimental results, we observe a pore- and ion-size dependent threshold-like charging behavior when the pore width becomes comparable to the size of the hydrated ion (0.65 nm pores for Na$^+$ and 0.79 nm pores for Cl$^-$ ions). The observed pore-size and potential dependent accumulation of ions in slit-shaped carbon pores can be explained by the hydration structure of the ions entering the charged pores. The results are discussed in view of their effect on energy-storage and desalination efficiency.

1. Introduction

Because of the intermittent nature of most renewable energy sources, including solar and wind, adequate energy-storage devices need to be deployed. As a complement to batteries, electric double layer capacitors (EDLCs) are attracting increased and significant attention. EDLCs store electrical energy by accumulation of ions at charged electrode–electrolyte interfaces,[1] combine high power density with long cycle life, and are generally built with environmentally friendly materials. The main drawback currently limiting the wide applicability of EDLCs is their still too low energy density.[2] A related technology is capacitive desalination (CD) that like EDLCs, relies on accumulation of ions in charged pores.[3] In CD the goal of the charge storage is not energy storage, but charge removal from the electrolyte. Understanding the behavior of aqueous electrolytes confined within narrow carbon-based pores at the molecular level is expected to help boost the performance of both EDLCs and CD cells.

Because the amount of energy/ions stored by EDLCs and CD cells scales with the available surface area, high surface area materials are typically used as electrodes. Porous carbons are often the material of choice as they combine high surface area with high electrical conductivity.[4] In EDLCs, a number of different electrolytes are used, including aqueous, organic, and ionic liquids.[5] Aqueous electrolytes typically offer higher power densities because of their high ionic mobility, while organic electrolytes offer higher energy densities because of

[a] *School of Chemical, Biological and Materials Engineering, The University of Oklahoma, Norman, OK 73019, USA. E-mail: astriolo@ou.edu*

[b] *Nanoscale Synthesis and Characterization Laboratory, Lawrence Livermore National Laboratory, Livermore, CA 94550, USA. E-mail: biener2@llnl.gov*

[c] *Stanford University, Department of Mechanical Engineering, Stanford, CA, USA*

† R. Kalluri and M. M. Biener contributed equally to this work.

This journal is © the Owner Societies 2013

Phys. Chem. Chem. Phys., 2013, **15**, 2309–2320 | **2309**

their wider electrochemical stability window.[2,4a] Chmiola et al.[6] showed that the capacitance of nanopores in non-aqueous electrolytes depends strongly on the pore size, and increases by a factor of 3 as the pores become smaller than the size of the solvated ion. This effect was attributed to a distortion of the ion solvation shell. This observation triggered a number of experimental studies on the development of advanced electrode materials,[7] and theoretical-experimental investigations to explain the behavior of electrolytes under confinement.[8] Molecular simulations were employed to quantify the energy barriers encountered by the ions as they enter narrow carbon-based pores from bulk solutions,[9] as well as ion–ion and ion–water correlations under confinement.[10] Other simulation studies focused on ionic liquids.[11] The results obtained by the synergism between experimental and theoretical approaches are likely to yield a better understanding of the behavior of electrolytes under confinement, which will promote significant advances in the EDLC cell design, as well as in other related applications like CD.[12]

Here we use a combination of experiments and molecular dynamics simulations to explore the pore size and potential dependent structure and distribution of aqueous electrolytes as they partition between bulk solution and nanopores. The goal is to better understand synergistic ion–pore correlations that may be used to improve the performance of EDLCs and CD cells.

2. Experimental and simulation methods

2.1 Materials and electrochemical testing

Nanocarbon foams were synthesized through the acid-catalyzed sol–gel polymerization of resorcinol with formaldehyde to produce organic gels which are dried and subsequently carbonized in an N_2 atmosphere (1050 °C for 3 h).[13] The material has slit-shaped micropores with a size distribution that can be controlled by activation in a CO_2 atmosphere at 950 °C.[14] Mass-specific surface areas were measured with an ASAP 2020 Surface Area Analyzer (Micromeritics Instrument Corporation) based on the Brunauer–Emmett–Teller (BET) method, and micropore size distributions were calculated using MicromeriticsDFTPlus v3.01 software. All electrochemical experiments were performed in three-electrode cells using a Ag/AgCl reference electrode. The same nanocarbon foam was used as a counter electrode for cyclic voltammetry measurements, and a Pt foil counter electrode (∼3 × 5 cm) was used for electrochemical impedance spectroscopy measurements. The typical size of the working carbon electrode was 5 × 5 × 1 mm.

Cyclic voltammetry (CV) was used to study the effect of the width of the applied potential window on the charging/discharging behavior, and both area specific and gravimetric capacitance were calculated from the measured current response. The capacitance values reported below were obtained from the charging/discharging currents at 0 V (vs. Ag/AgCl). The main purpose of the current electrochemical impedance spectroscopy (EIS) experiments was to assess the very low-frequency charging/discharging behavior to better differentiate between kinetic and thermodynamic effects.

The capacitance values derived from EIS experiments were obtained from the measured imaginary component of the impedance Z_{im} using the correlation $C = -1/(2\pi f Z_{im})$, where f is the frequency.[1b] More details regarding the analysis and experimental setup used in EIS experiments can be found in a forthcoming publication.[15]

2.2 Methods and algorithms – simulations

The distribution of aqueous NaCl and $CaCl_2$ electrolytes in slit-shaped graphitic carbon electrodes was studied by equilibrium molecular dynamics simulations as a function of pore width and charge density. Extensive analysis on the structure of the electrolytes within the pores is provided in a separate contribution.[16] The simulation box (Fig. 1) is similar to that used in our prior work,[10a] and consists of two identical slit-shaped pores formed by two graphite slabs stacked along the Z direction. Each graphite slab consists of five graphene layers with an interlayer spacing of 0.335 nm, and X and Y dimensions of 2.24 and 2.13 nm, respectively. Periodic boundary conditions are implemented along all three directions. To incorporate the bulk properties of the electrolyte, the graphene layers are discontinuous in the Y direction. Pore widths, defined as center-to-center distance between the outermost carbon atoms of opposite graphite slabs, range from 0.65 to 1.6 nm.

The model for the carbon pores used for our simulations is a simplification of the experimental system. Explicitly, the pore shape considered in our simulations is always that of a slit pore, while experimental carbons clearly contain pores of many different types and shapes. We do not account for defects and chemical heterogeneities, and the simulated pores are not interconnected. More realistic representations of active carbons can be found in the literature,[17] but absolutely reliable models for a carbon adsorbent is not yet available. We consider our model a compromise that is simple enough to allow us to reach data in acceptable times, yet reliable enough to allow us to
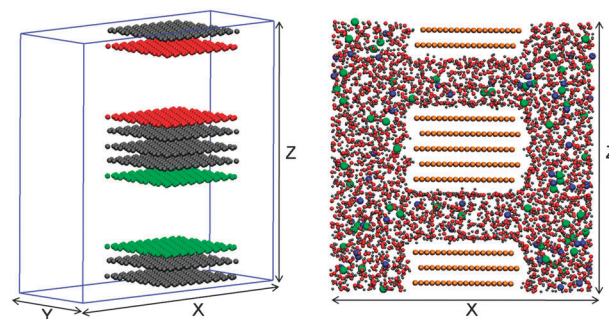

Fig. 1 Left: Schematic of the simulation box showing ten graphene layers, organized in two graphitic slabs. Two carbon-slit pores separate the graphitic slabs. Grey spheres represent neutral carbon atoms; green spheres represent carbon atoms that can bear partial positive charges to mimic the application of external voltages. Red spheres represent carbon atoms that can bear negative partial charges. Ions and solvent molecules are not shown for clarity. Right: Representative snapshot of the simulated system with neutral pores of width 1.6 nm. Orange spheres represent carbon atoms, blue spheres represent sodium ions, green spheres represent chloride ions, oxygen and hydrogen of water are shown as red and grey spheres, respectively.

Table 1 Summary of simulation parameters

System	Pore width (nm)	Water molecules	Na$^+$ ions	Ca^{2+} ions	Cl$^-$ ions	Ionic strength
1	1.6	1670	54	0	54	1.80 M
2	1.2	1670	54	0	54	
3	0.9	1670	54	0	54	
4	0.79	1670	54	0	54	
5	0.7	1670	54	0	54	
6	0.65	1670	54	0	54	
7	1.6	5000	0	54	108	
8	1.2	5000	0	54	108	
9	0.9	5000	0	54	108	
10	0.79	5000	0	54	108	
11	0.7	5000	0	54	108	
12	0.65	5000	0	54	108	

investigate the effect of pore size and that of applied voltage on the measured capacitance.

The sodium (Na$^+$) and chloride (Cl$^-$) ions were modeled as charged Lennard-Jones spheres by employing the parameters proposed by Dang and collaborators,[18] calcium (Ca^{2+}) ions were modeled as charged Lennard-Jones spheres as proposed by Predota et al.[19] Water was modeled using the simple point charge extended (SPC/E) model.[20] Carbon atoms were modeled as Lennard-Jones (LJ) spheres with parameters taken from Cheng and Steele.[21] All simulations were conducted using the package LAMMPS in the NVT ensemble.[22] The compositions of the systems simulated are summarized in Table 1. Other details are available in ref. 10a,16. Unless specified, all simulations were performed at 300 K, and the system was designed to reproduce the liquid density of water at ambient conditions in the simulation region outside of the pores.

Charging of the electrode–electrolyte system was simulated by uniformly placing charges on the interfacial carbon atoms. Charge densities studied range from 0 (neutral pores) to 15 μC cm^{-2} (~0.024 electron per carbon surface atom). Carbon surfaces facing one pore bear charges of the same sign. Explicitly, the bottom pore in Fig. 1 has positively charged surfaces, while the top pore carries the same amount of charge but of the opposite sign to maintain electro-neutrality. High ionic strength (1.8 M) was chosen to avoid significant ion depletion outside of the charged pores.[23]

Our molecular dynamics simulation results are complementary to others, available in the literature, obtained using Monte Carlo methods. Two contributions are particularly important for the present work. Yang et al.[24] showed that within carbon-slit nano-pores predictions of the formation of the electric double layer based on the continuum Guoy–Chapman model fail to reproduce Monte Carlo simulation results based on the primitive model, which treats water molecules implicitly. Further, in the same contribution Yang et al. showed that when water molecules are described explicitly, the structure of the aqueous electrolyte system differs compared to that obtained using the primitive model. These observations justify the need of considering explicitly water molecules in simulating the system of interest here. To investigate the equilibrium partition of ions within charged pores it would be preferable to implement the grand canonical Monte Carlo algorithm. However, as pointed out by Yang et al. and also by Hou et al.,[25] the acceptance rate would be extremely low should an explicit model be used to describe water molecules.

3. Results and discussion

3.1 Electrochemical experimental characterization

We performed electrochemical tests on two nanocarbon foams that displayed a similar macroporous 3D morphology (Fig. 2a) but differed in their micropore size distributions (Fig. 2b). Both materials were prepared from the same polymer precursors that determined their macroporous morphology. The micropore size distribution in the electrodes was tuned by thermal activation, a process that involves controlled burn-off of carbon from the foam. The activation process creates new slit-shaped micropores and, therefore, increases the overall surface area of the foam (from 480 m^2 g^{-1} for the non-activated material to
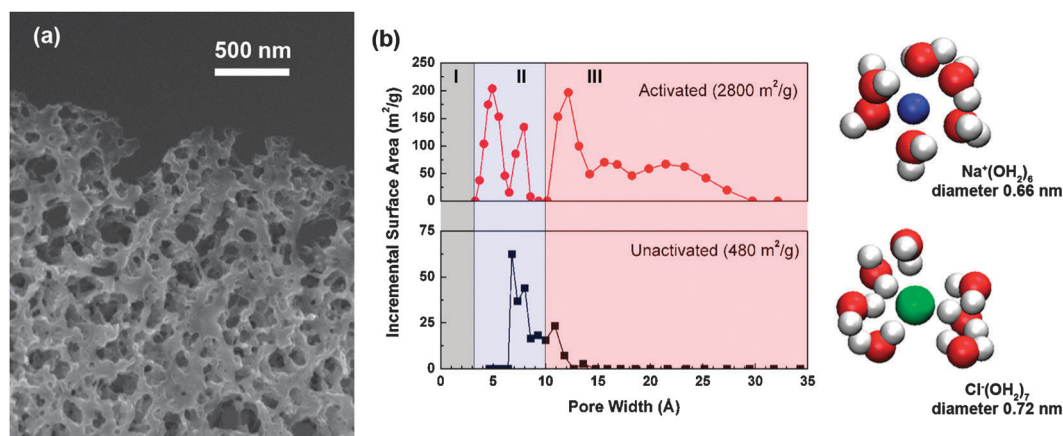

Fig. 2 Polymer derived graphitic nanocarbon foams: (a) Scanning electron micrograph showing the characteristic macroporous morphology, and (b) comparison of the micropore size distributions of non-activated and activated samples (BET surface areas of 480 and 2800 m^2 g^{-1}, respectively) as determined from N$_2$ adsorption isotherms using the density functional theory (DFT) method. The non-activated nanocarbon foam is dominated by wettable sub-nm pores (region II) that are similar in size to hydrated sodium (diameter d ~ 0.66 nm, coordination number cn ~ 6.2) and chloride ions (d ~ 0.72 nm, cn ~ 7.1).

values in excess of 2800 m^2 g^{-1}).[14] For the materials investigated here, thermal activation broadens the micropore size distribution, from 0.7–1.1 nm for the non-activated samples to 0.4–3 nm for activated samples. Importantly, activation of the material also significantly increases the fraction of overall surface area that is attributable to pores larger than 1 nm (region III in Fig. 2b). Further, the widths of the sub-nm micropores in the non-activated nanocarbon foam (region II in Fig. 2b) are similar to the sizes of hydrated Cl$^-$ (diameter $\sim$0.72 nm), Na$^+$ ($\sim$0.66 nm), and Ca^{2+} ions ($\sim$0.7 nm) used in the simulations discussed below.[26] It should be pointed out that simulation studies suggest spontaneous dewetting for neutral carbon-based slit-shaped pores within region I.[10b]

Our CV experiments reveal that the micropore size distribution has a pronounced effect on the charging/discharging behavior of nanocarbon foams in aqueous electrolytes (Fig. 3). CV curves obtained from activated samples are characteristic of ideal (linear) capacitive behavior, as demonstrated by their rectangular shape and the fact that the charging/discharging currents are independent of the width of the applied potential window (Fig. 3b). In contrast, CV traces collected from non-activated samples strongly deviate from the ideal rectangular shape (Fig. 3a). Furthermore, the charging/discharging currents, and thus the capacitance C (Fig. 3c), increase by more than 1 order of magnitude, from a few F g^{-1} for narrow potential sweep ranges (smaller than -0.3 to 0.3 V $vs.$ Ag/AgCl) to $\sim$40 F g^{-1} for wider potential sweep ranges (-0.9 to 0.9 V $vs.$ Ag/AgCl). The transition between the low and high capacitance region is relatively abrupt and is marked by the appearance of a peak in the negative-sense sweep. This unexpected result suggests that the capacitance of sub-nm pores is strongly potential dependent in $addition$ to the increase

of capacitance in sub-nm pores reported by Chmiola et $al.$[6] The latter effect, an increase of the area-specific capacitance C_A with decreasing pores size, is observed in wide potential sweeps. For example, for wide sweeps, the C_A of the non-activated material approaches $\sim$8 µF cm^{-2} (40 F g^{-1}), which is 2 to 3 times the C_A of activated material (3–4 µF cm^{-2}). Similar results were obtained by potential step experiments (data not shown). By contrast, the capacitance measured for the activated carbon pores ($\sim$100 F g^{-1}) did not depend on the applied potential sweep.

Previously, Yang et $al.$[27] reported CVs from carbon aerogel electrodes in dilute NaF electrolytes that showed a capacitance minimum similar to that observed in the wide potential window scans shown in Fig. 3a. The authors explained the observation of this capacitance minimum by the classical electrical double-layer theory. The theory predicts that pores those size is smaller than a specific value (the so-called cutoff pore width) do not contribute to the total capacitance because of electrical double-layer overlapping.[28] The double-layer thickness, and thus the cutoff pore width decreases with increasing electrolyte concentration and potential. For example, the cutoff pore width for a 0.0024 M NaF electrolyte and 1.2 V applied voltage was calculated to be $\sim$0.6 nm, and its value further decreases with increasing electrolyte concentration.[28] Thus, although the classical model seemingly explains the pore- and potential dependent charging behavior of carbon electrodes in very dilute electrolytes, it definitely fails to describe the charging behavior at the high electrolyte concentrations (Fig. 3a) used in the present study.

An atomistic interpretation of the potential dependent charging behavior of the unactivated material is that ions entering sub-nm-pores have to strip off (or at least deform)
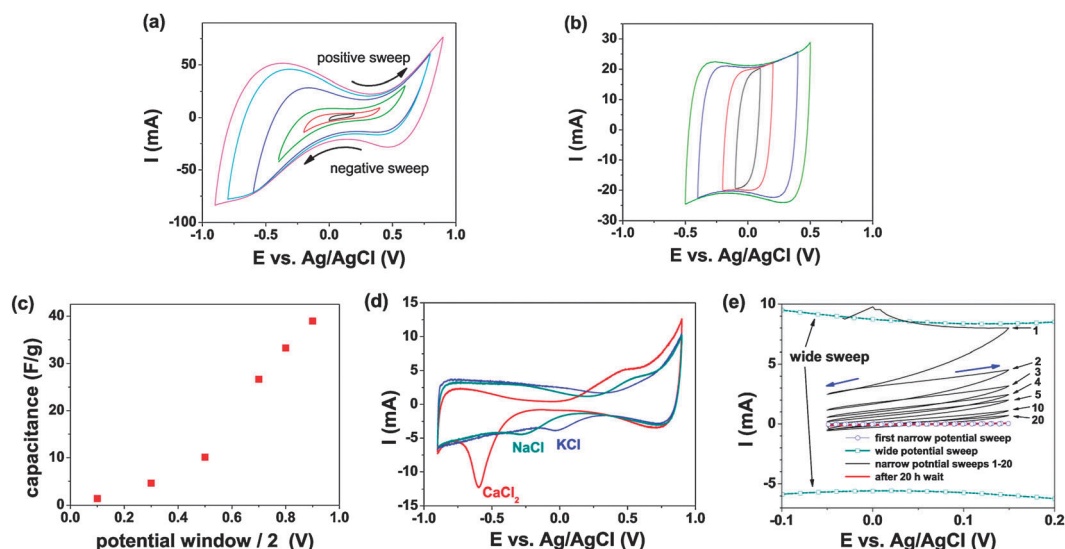

Fig. 3 Effect of pore size distribution, potential window, and hydration shell strength on the charging/discharging behavior of nanocarbon foams: CVs collected from (a) non-activated (10 mV s^{-1}) and (b) activated (10 mV s^{-1}) samples as a function of the width of the applied potential window; (c) gravimetric capacitance $vs.$ width of the applied potential window calculated from the CVs shown in panel (a); (d) CVs collected from a non-activated sample (0.5 mV s^{-1}) demonstrating the effect of the hydration shell strength of cations on the charging/discharging behavior; (e) transient behavior of CVs (10 mV s^{-1}) obtained from non-activated material in a narrow potential window around 0 V after performing wider potential sweeps.

part of their hydration shell and that this can only happen if the electrochemical driving force is large enough to offset the associated energy penalty. Once this condition is met, the area specific capacitance of sub-nm pores increases sharply, and surpasses that of the larger pores present in the activated material. To test this hypothesis, we studied the effect of the strength of the cation hydration shell and ion size on the charging/discharging behavior by exchanging Na^+ with K^+ or Ca^{2+}. The hydration free energy and the hydrated ion radius each change for these species. We observe that the peak that marks the transition from low to high capacitance values shifts towards more negative potentials and becomes more pronounced as the strength of the hydration shell increases (Fig. 3d). This peak shift is not correlated to changes in the limiting ionic conductivities (Na^+ 50.1, $1/2 Ca^{2+}$ 59.5, K^+ 73.5, all in 10^{-4} m^2 S mol^{-1}),[29] nor to the radii of the bare ions in solution (Na^+ 0.097 nm $<$ K^+ 0.141 nm $<$ Ca^{2+} 0.173 nm),[30] but instead correlates with the hydration free energies (K^+ 295 kJ mol^{-1} $<$ Na^+ 365 kJ mol^{-1} $<$ Ca^{2+} 1504 kJ mol^{-1}).[31] Despite these relatively high values of the hydration free energies, the binding energy of individual inner shell water molecules is quite small. For example, even for a strongly hydrated ion such as Ca^{2+} the binding energy of an individual inner shell water molecule can be as low as $\sim$70 kJ mol^{-1}.[32] Thus, although the applied electrochemical driving force is not strong enough to cause complete loss of the hydration shell, it likely can induce sufficient perturbations on the hydration shell that would allow the ion to penetrate the charged pores. These trends are consistent with the simulation results of Yang and Garde which suggested that the selectivity of aqueous cations to enter negatively charged carbon nanotubes depends on the ions hydration free energy.[9b]

To assess whether the observed dependence of the capacitance on the width of the potential window is kinetically or thermodynamically controlled, we measured the charging/discharging behavior in a narrow potential window around 0 V after performing wider potential sweeps. We observed that the charge/discharge currents (and thus the capacitance) decrease over time until they are identical to those originally measured *before* performing a wide potential sweep (Fig. 3e). This observation suggests that ions which entered the sub-nm pores during the wide sweep were not thermodynamically stable in sub-nm pores and their depletion starts as soon as the chemical potential driving force is removed. If, on the other hand, the effect would be caused by a kinetic free energy barrier encountered by ions entering sub-nm pores, one would expect that the capacitance remains high if the chemical potential driving force is removed.

Electrochemical impedance spectroscopy (EIS) results from non-activated and activated nanocarbon foams are compared in Fig. 4. Impedance was measured at frequencies from 10 kHz to 10 mHz and potentials from −0.5 to 0.5 V *vs.* Ag/AgCl. Each sample shows the expected decrease of capacitance with increasing frequency,[1b] but they differ in their potential dependence. The activated material shows very little variation in *C vs. f* curves when we changed the electrode potential,
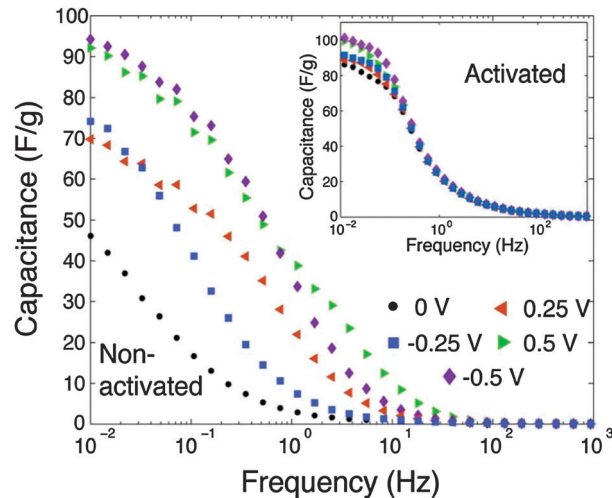

Fig. 4 Capacitance *vs.* frequency behavior for non-activated and activated nanocarbon foams (5 × 5 × 1 mm) at different potentials. The EIS measurements were performed in 2.5 M NaCl, with a frequency scan from 10 kHz to 10 mHz, and a voltage amplitude of 5 mV.

consistent with the CV data shown in Fig. 3 and with the expected behavior for an ideal linear capacitor. In contrast, EIS data for the non-activated sample shows a pronounced effect of the potential on the capacitance-frequency relationship. In the limit of very low frequencies (10^{-2} Hz), which should reflect equilibrium capacitance values, the capacitance increases about 2 fold as the potential changes from 0 to ±0.5 V, reflecting the charging/discharging currents observed in CVs for wide potential windows. At 1 Hz (corresponding to a mean scan rate of 20 mV s^{-1}, comparable to the scan rates used in the CVs shown in Fig. 3) the increase in capacitance becomes more pronounced, from $\sim$3 F g^{-1} at 0 V to $\sim$40 F g^{-1} at ±0.5 V. Since the ion conductivity and pore structures remain constant, the change in capacitance at 1 Hz seems to be partially caused by kinetic effects due to chemical potential gradients. Indeed, the *C–f* curves shown in Fig. 4 reveal that the 1 Hz region already falls into the frequency region where kinetic effects become important. Importantly, the behavior reflects the strong increase of the charging/discharging currents with increasing width of the potential window observed in the CVs obtained from non-activated foam samples (Fig. 3a).

In summary, our experimental results suggest that the higher capacitance observed for sub-nm pores (8 µF cm^{-2} for the non-activated material *vs.* 3–4 µF cm^{-2} for the activated material) comes with an energy penalty encountered by the hydrated ions as they enter the pores (and perturb their hydration shells) that can only be overcome if the chemical potential driving force is large enough. This effect seems to be caused by a combination of thermodynamic and kinetic effects.

3.2 Simulated bulk-pore ions partition

Molecular dynamics simulations were used to quantify the equilibrium partition of ions inside the charged pores. The results were quantified in terms of the concentration of ions
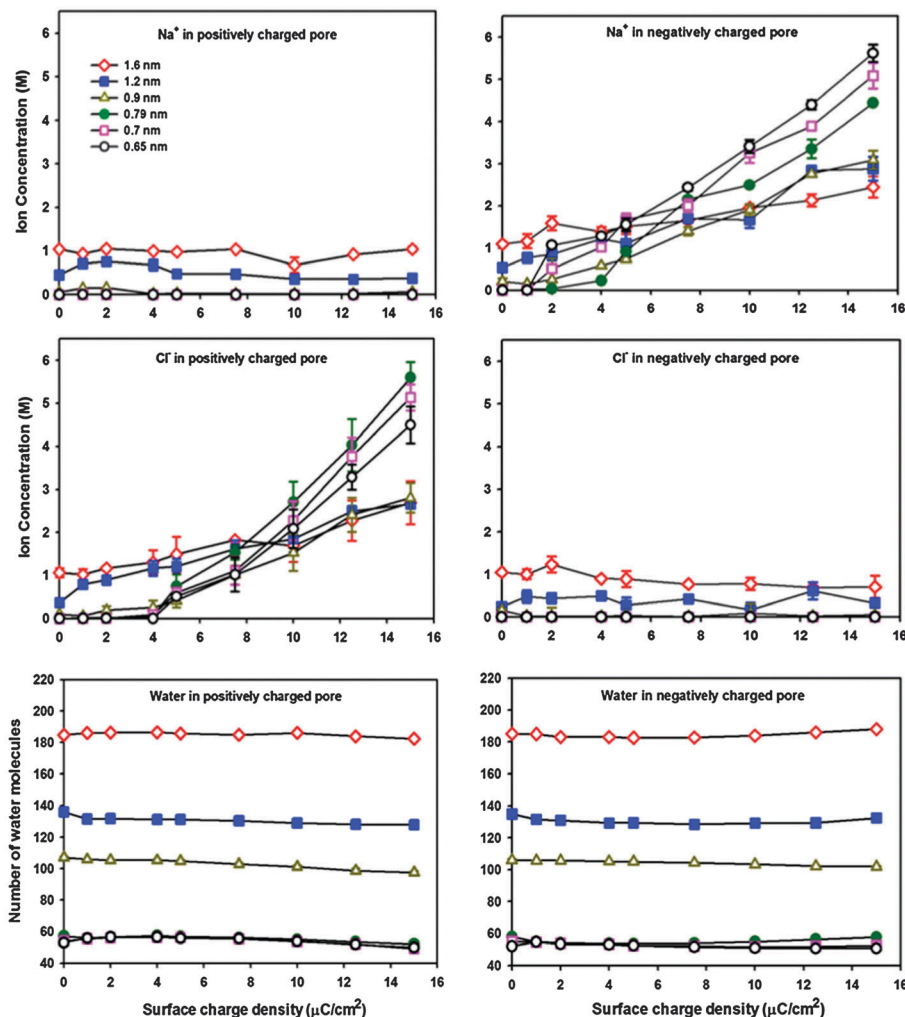
Fig. 5 Average concentration of sodium (top panels) and chloride ions (middle panels) and average number of water molecules (bottom panels) found within the simulated pores as a function of the surface charge density. Results obtained for pores of width 1.6, 1.2, 0.9, 0.79, 0.7, and 0.65 nm are represented by empty diamonds, full squares, empty triangles, full circles, empty squares, and empty circles, respectively. The panels on the left are for positively charged pores, those on the right for negatively charged ones. Lines are guides to the eye. Error bars for data in the bottom panels are smaller than the symbols.

inside the pores as a function of pore width and charge density. The results are summarized in Fig. 5 for aqueous NaCl solutions, and in Fig. 6 for aqueous $CaCl_2$ solutions. Simulations were conducted at ambient conditions. The results are generally consistent with the observation that to enter smaller pores, or to approach the pore surface in the wider pores, the ions must lose part of their hydration shell, which is energetically unfavorable. Free energy barriers encountered during this process, not detailed herein but available in the literature, are likely to slow the process dynamics. Note that the current simulation is not accurate for comparing kinetics data to experimental observations (e.g., we expect that in real porous carbons oxygen-containing defects are present at pore entrances, which would affect the kinetics of ions adsorption). The results discussed below are in general consistent with our prior results,[10a] with the analysis of simulation results for carbon-slit pores[9a] and for carbon nanotubes,[9b] as well as with classical thermodynamic arguments.[8a]

The results in Fig. 5 show that the concentration of sodium ions within negatively charged pores (top right panel), and chloride ions within positively charged pores (middle left panel) increase as the surface charge density increases. These results are qualitatively consistent with experimental data reported by Mueller and Kastening[33] for various electrolytes in carbon-based pores of width ~1.2 nm (value obtained assuming slit-shaped pores) or ~4 nm (assuming cylindrical pores). Mueller and Kastening observed a decrease in the bulk electrolyte concentration upon polarizing the carbon electrodes in EDLCs, probably due to the accumulation of the electrolytes within the pores. We note, however, that in all simulated cases only a limited number of ions penetrate the pores. Our simulations also show that, in general, more ions are found within the larger pores (although at lower concentrations) than within the narrow ones. At the highest surface charge densities considered, the number of ions in narrow pores can be 0.5 times that of wider pores. As a consequence, the degree of surface charge
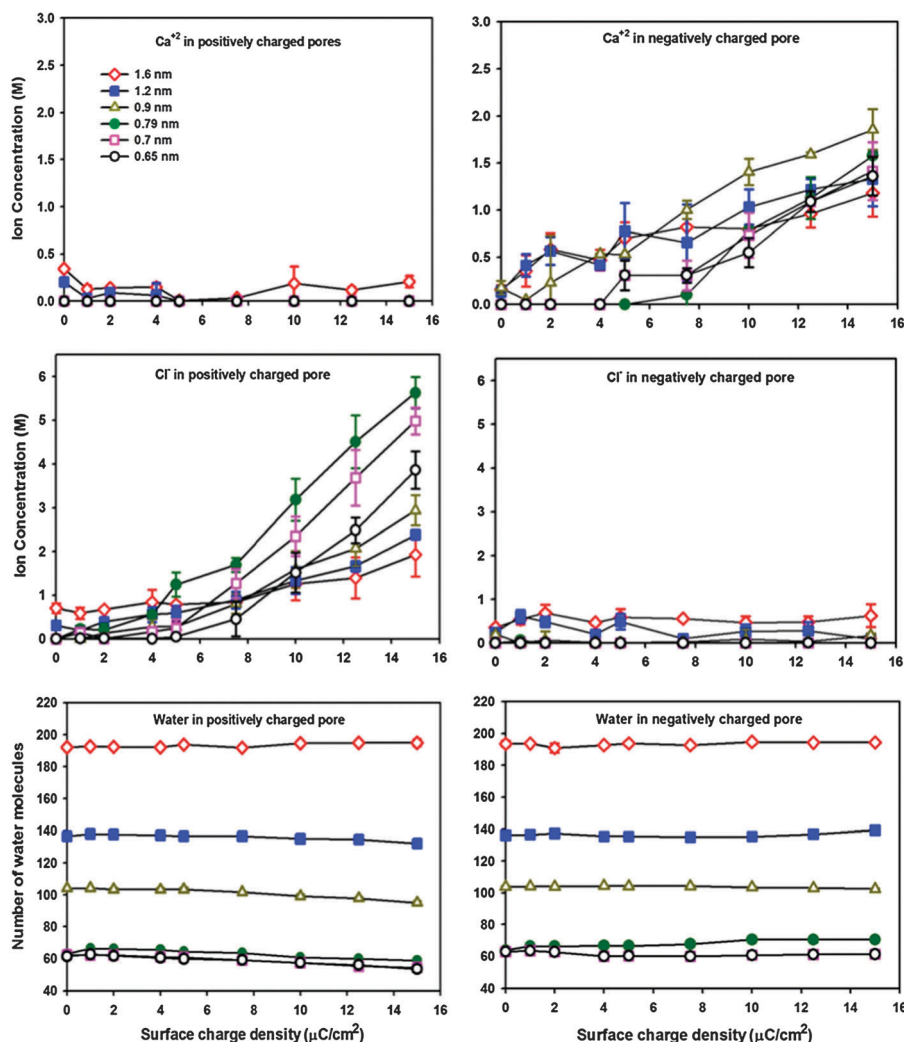
Fig. 6 Average concentration of calcium (top panels) and chloride ions (middle panels) and average number of water molecules (bottom panels) found within the simulated pores as a function of the surface charge density. Results obtained for pores of width 1.6, 1.2, 0.9, 0.79, 0.7, and 0.65 nm are represented by empty diamonds, full squares, empty triangles, full circles, empty squares, and empty circles, respectively. The panels on the left are for positively charged pores, those on the right for negatively charged ones. Lines are guides to the eye. Error bars for data in the bottom panels are smaller than the symbols.

compensation is higher in the wider pores than it is in narrower ones. At the highest surface charge densities, the concentration of counter-ions in sub-nm pores is a factor of 2 higher than that found in wider pores. This gain in volumetric capacitance may make the non-activated material interesting for single-pass desalination of higher salinity solutions although the lower degree of charge compensation in the narrow pores of this material will negatively affect the energy efficiency of CD cells.

To quantify the observations regarding the surface charge compensation summarized above, in Fig. 7 we report: (a) the net pore charge in positively- and negatively-charged pores as a function of charge density (top left and right panels, respectively); and (b) the density distribution of Cl^- ions observed along a plane perpendicular to the pore surface for positively charged pores of width 0.65 and 1.6 nm with surface charge density of +15 μC cm^{-2} (bottom left and right panels, respectively). The net pore charge is the difference between the charge

stored on the pore surface by the applied surface charge density and the charge stored in the pore volume by the electrolyte (number of counter-ions minus the number co-ions). The analysis (Fig. 7, top panels) reveals that the applied surface charge is not completely compensated by the ions accumulated in the pores, and that the degree of charge compensation in narrower pores is lower than that in wider pores. Complete charge compensation is only observed for wider pores at low surface charge densities. The density profiles shown in the bottom panels of Fig. 7 show unambiguously that ions enter wider pores much more easily that they do the narrow ones. Further, in the case of the narrow pores there is evidence of ions accumulation at the pore entrance, where the ions need to strip some of the hydration water if they are to penetrate the charged pores.

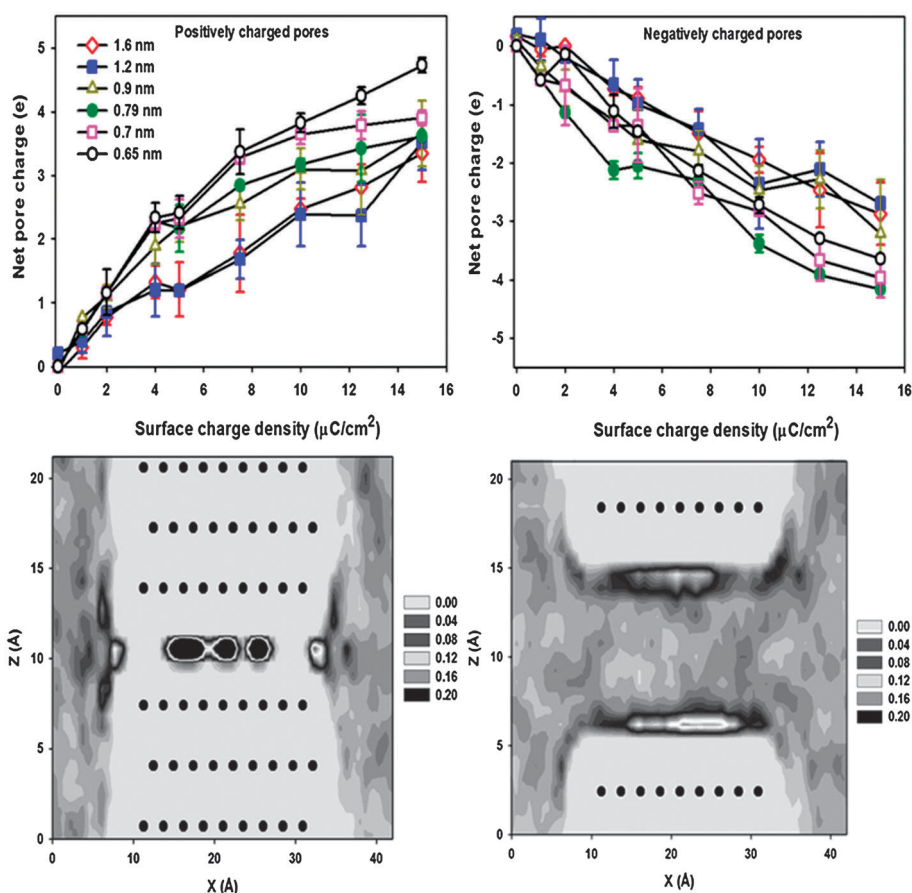Important for comparing results in Fig. 5 to the experimental data above is that the small pores (e.g., 0.65 nm wide)

Fig. 7 *Top panels*: Net pore charge for the various positively (left) and negatively (right) charged pores as a function of the surface charge density. Results are obtained at ambient conditions for NaCl electrolytes. Different symbols are for pores of different widths. Empty diamonds, full squares, empty triangles, full circles, empty squares, and empty circles represent results for pores of width 1.6, 1.2, 0.9, 0.79, 0.7, and 0.65 nm, respectively. The net pore charge is the difference between the charge stored on the pore surface by the applied charge density and the charge stored in the pore volume by the electrolytes (number of counter-ions minus the number of co-ions). *Bottom panels*: Planar density profiles along a plane perpendicular to the pore surface for Cl^- ions interacting with one pore of width 0.65 nm (left) and one pore of width 1.60 nm (right). Both pores are positively charged with surface charge density +15 μC cm^{-2}. The carbon atoms are shown as black dots to identify the position of the pore surfaces and of the pore entrance. Ion densities are expressed in atoms per cubic Å.

are inaccessible to Na$^+$ ions until the surface charge density is larger than 4 μC cm^{-2}, and that pores of width 0.79 nm or smaller are inaccessible to Cl$^-$ ions until the surface charge density is larger than ~5 μC cm^{-2}. As the surface charge density increases above these values, these narrow pores can be filled by ~4 ions at the largest surface charge density observed. The wider pores (*e.g.*, see data for the 1.6 nm wide pores) contain ~4 NaCl ion pairs when the surface charge density is 0. As the surface charge density increases in the wider pores, more counter-ions are adsorbed. These simulation results are consistent with the trends observed in experiments which suggest that the ion penetration into sub-nm pores requires a high surface charge density to overcome the energy penalty associated with disrupting (or at least perturbing) the hydration shell. Once the driving force becomes large enough, ions accumulate within the narrow pores, where they can simultaneously interact with both charged surfaces across the pore volume. Note that the results in Fig. 5 describe the equilibrium partition of ions inside the various pores. Although our simulations suggest that, in agreement with the

interpretation of the experimental data, the potential dependent capacitance of sub-nm pores is controlled by thermodynamics, kinetic data are not available at the level of accuracy that would allow us to rule out dynamics effects as responsible for experimental observations. Our equilibrium results suggest that the ionic concentration inside the charged narrow pores can be a factor of two larger than that inside the wider pores considered, consistent with our hypothesis that narrow pores can improve the volumetric capacitance of EDLCs and CD cells, provided large enough voltages are applied.

Our results suggest that the ions hydration strength dictates their ability to enter narrow pores. Simulation results by Shao *et al.*[34] show that as the temperature increases the coordination (*e.g.*, relative orientation, indicative of preferential electrostatic interactions) between water molecules in the first hydration shell and sodium ions decreases, suggesting a decrease in the hydration strength. As a consequence, one would expect an increase in the ion concentration inside narrow charged pores at low surface charge densities when the simulations are conducted at high temperatures because the hydration shell

2316 | *Phys. Chem. Chem. Phys.,* 2013, **15**, 2309–2320

This journal is © the Owner Societies 2013

is expected to be more easily perturbed under those conditions. To test this hypothesis we conducted one simulation for the pores of width 0.79 nm at the surface charge density of 4 $\mu C\ cm^{-2}$. For these pores it was found that at 300 K the Na^+ and Cl^- concentrations inside the negative and positive pores are 0.19 $\pm$ 0.06 and 0.042 $\pm$ 0.004 times their bulk concentrations, respectively. These ratios increase to 0.43 $\pm$ 0.11 and 0.19 $\pm$ 0.05, respectively, when the temperature is 348 K, suggesting that increasing the temperature could increase the capacitance in materials with narrow pores. It should also be pointed out that, as the pore width decreases below the size of the non-hydrated ion, excluded volume effects prevent the ions from entering the pores, precluding further enhancements in the EDLCs energy density.

The results in Fig. 5 also show that a few sodium ions can be found within the positively charged pores (top left panel), and a few chloride ions within the negatively charged pores (middle right panel), although only within the wider pores considered. This suggests that ion–ion correlations could be important in determining the EDLCs and the CD cells behavior, but mostly in wide pores. For completeness, we also report in Fig. 5 (bottom panels) the number of water molecules found within the various pores. For all pores simulated in aqueous NaCl and surface charge densities equal to or lower than 7.5 $\mu C\ cm^{-2}$, the number of water molecules in positively charged pores is slightly larger than that in negatively charged pores. For surface charge densities of 10 $\mu C\ cm^{-2}$ and above, the opposite is observed. Although the differences are small, by conducting additional simulations in which no ions were present (not discussed here for brevity), we concluded that these differences are due primarily to the different size and hydration of Na^+ and Cl^- ions, which are confined within the charged pores.

To further address the effect of hydration strength on the CVs data shown in Fig. 2, we repeated the simulations just discussed with a $CaCl_2$ electrolyte at equal ionic strength (1.8 M). The data obtained are shown in Fig. 6. The results are qualitatively similar to those obtained for NaCl, but some important differences are noted. In particular, our results confirm that higher surface charge densities are required for the Ca^{2+} ions to enter the narrow pores, in agreement with the experimental observations discussed above, and our results also suggest that the pores of size $\sim$0.9 nm or wider are suitable to maximize the concentration of confined Ca^{2+} ions at high surface charge densities. The concentration of confined Cl^- is qualitatively similar to those discussed in Fig. 5, although it is interesting to note that fewer Cl^- ions enter the positively charged pores when $CaCl_2$ solutions are considered, probably because of electrostatic effects in the bulk solutions, and possibly because the concentration of Cl^- ions in the $CaCl_2$ system is much lower than that considered in the NaCl electrolyte. It should also be pointed out, for completeness, that the simulations conducted for aqueous $CaCl_2$ solutions are affected by higher statistical uncertainty due to the difficulty encountered by the Ca^{2+} ions to lose water molecules from their hydration shells and enter the charged pores.

The capacitance depends not only on the concentration of the electrolytes within the charged pores, but also on their distribution near pore surface. To contrast the effect of pore size on the equilibrium distribution of ions within the charged pores, in Fig. 8 we report axial density profiles for Na^+, Cl^-, and oxygen atoms of water within charged pores of width 1.6 (top panels) and 0.65 nm (bottom panels). The panels on the left are for positively charged pores, those on the right for negatively charged ones. In all cases, the surface charge density is 12.5 $\mu C\ cm^{-2}$. In wider pores, water molecules yield four layers, while only a single layer of water molecules is observed within the narrower pores considered in Fig. 8. The details regarding the density distribution of oxygen atoms of water molecules change when pores of the same width are either negatively or positively charged (compare left to right panels). This is a consequence of the different orientation of confined water, dictated by the surface charge density. Within the positively charged 1.6 nm-wide pores, our results suggest that Cl^- ions accumulate at and contact with the positively charged surfaces (top left panel), yielding a density maximum just above the first hydration layer. On the contrary, Na^+ ions within the negatively charged pores (top right panel) accumulate slightly further from the negatively charged surfaces, yielding a density maximum in correspondence of a region depleted of water molecules. We attribute this to the strength of the hydration shell for the two ions considered. While Cl^- ions easily lose part of their hydration shell, Na^+ ions prefer to maintain it. The distribution of the ions within the narrow pores differs significantly compared to that just described. For example, in the bottom panels of Fig. 8 we show the density distributions within the 0.65 nm-wide pores. Cl^- ions within the positively charged pores (left) yield one layer at the center of the pore. On the other hand, Na^+ ions yield two adsorbed layers inside the negative pores, one near each of the charged surfaces. This different behavior is due primarily to the different size of the ions, but also to the strength of their hydration shells. Cl^- ions are so large that they can only fit at the center of the pore. Na^+ ions are a little smaller than Cl^-, so they do not need to be at the pore center. In addition, by adsorbing at contact with one of the charged surfaces, each Na^+ ion can maintain at least part of its hydration shell. Describing the results in Fig. 5 we pointed out that a few Na^+ (Cl^-) ions can be found inside wide positively (negatively) charged pores. The density distribution results in Fig. 8 show that these co-ions tend to accumulate at the center of the pores, far from the like-charged surfaces. Based on simulation results discussed elsewhere,[10a] we expect that these effects are due to ion–ion correlations. The results shown in Fig. 8 were obtained after equilibration was reached. No information was collected regarding the time required for the ions to enter the pores, nor the time spent, on average, by the ions inside the pores. It should be pointed out that such results would be strongly dependent on the details of the simulated system, and hence would perhaps be not widely applicable. We also point out that the relation between the strength of hydration and ion pairing has been studied for bulk systems in extreme environments.[35] We are currently investigating how such phenomena are altered under confinement.

In summary, the simulation results corroborate the experimental findings, in that high surface charge densities are necessary for allowing aqueous electrolytes to penetrate narrow
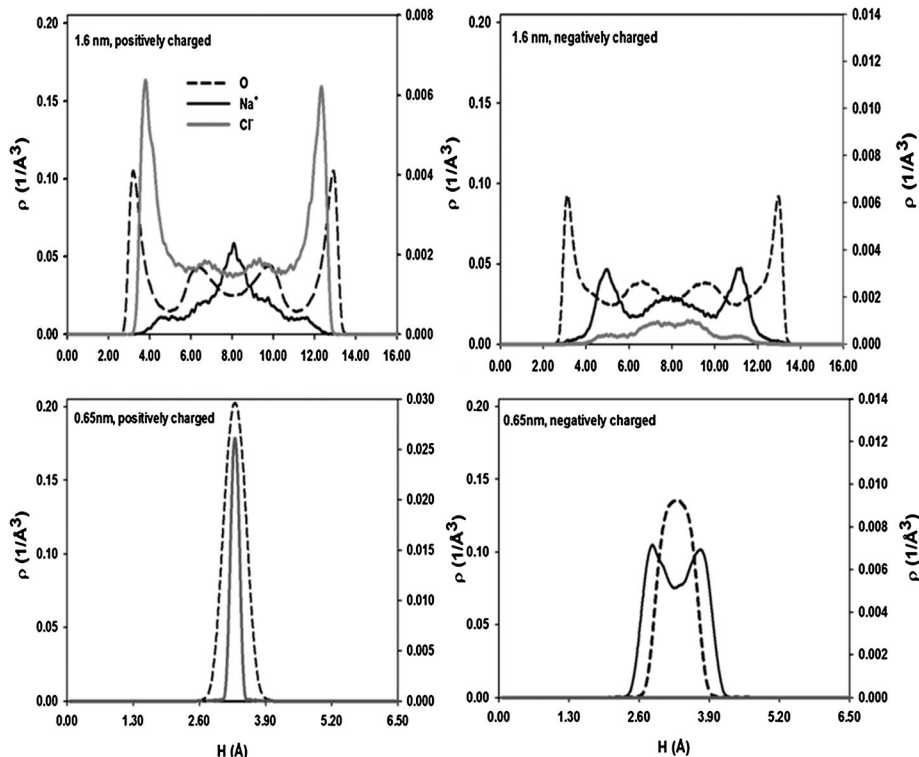
Paper

Fig. 8 Density profiles for oxygen of water (dashed black), sodium (continuous black), and chloride ions (continuous grey) within slit-shaped pores at surface charge density 12.5 µC cm^{-2}. Atomic oxygen densities are shown in the left Y axes, atomic densities for ions are shown in the right Y axes. The top panels are for results obtained in for pores of width 1.6 nm; the bottom panels for results obtained in pores of width 0.65 nm. The panels on the left are for positively charged pores, those on the right for negatively charged ones. The vertical distance from the pore surface, H, is measured from the center of the carbon atoms.

pores. Our simulations suggest that increasing the temperature might lead to higher capacitance for carbon materials with narrow pores, and that it might be possible to maximize the EDLC energy density by employing electrodes with different pore size distributions, depending on the electrolytes used. The results in Fig. 8 suggest that the propensity of electrolytes to lose their hydration shell upon confinement depends not only on pore width, but also on ion type and both pore–water and ion–water correlations.

4. Conclusions

In summary, through a combination of electrochemical experiments and molecular dynamics simulations, we have observed pronounced pore size effects on the capacitance of nanocarbon foam electrodes that go beyond those previously reported for organic electrolytes. Specifically, we have observed a pore and ion-size dependent threshold-like charging behavior in pores whose width is smaller, yet comparable to the size of the hydrated ions. Ions that enter these sub-nm-pores have to partially deform their hydration shell, and this can only occur if the chemical potential driving force is large enough to offset the associated energy penalty. Increasing the temperature might facilitate distortion of the hydration shell, possibly yielding higher capacitance.

The concentration of cations within negatively charged pores, and anions within positively charged pores increases

as the applied surface charge density increases. Complete charge compensation, however, is only observed for wider pores at low surface charge densities. For higher charge densities, the wall charge is only partially compensated by the ions accumulated in the pores, and the degree of charge compensation is lower in narrow pores than that in wider pores. Our results also show that higher surface charge densities are required for the ions to enter the smaller pores. Thus our results show that the performance of EDLC and CD cells depends not only on pore size, but also on the applied voltage. As previously reported by Chmiola *et al.*,[6] and confirmed by our experiments, the area-specific capacitance of sub-nanometer pores surpasses that of larger pores. The effect has been explained by the distortion of the solvation shell of ions entering sub-nm pores, which leads to smaller ion-electrode separation. The resulting higher capacitance increases the energy storage capacity of EDLCs and can potentially increase the desalination performance of CD cells by leading to higher counter-ion concentrations in sub-nm pores. On the other hand, the gain in storage capacity of ions in sub-nm pores could come with an efficiency penalty as the degree of charge compensation is lower in narrow pores, and the energy that is necessary to distort the solvation shell adds to electrical work needed to charge the EDLC or CD cell. The latter effect may appreciably decrease the energy efficiency if the energy that is stored in the distortion of the solvation is not recovered during discharging, and instead dissipated as heat. On the other hand, this heat might

2318 | *Phys. Chem. Chem. Phys.*, 2013, **15**, 2309–2320

This journal is © the Owner Societies 2013

enhance the device performance as our simulations suggest that increasing the temperature facilitates the ability of ions to enter narrow pores. The effect should be more pronounced for ions with a relatively rigid solvation shell whose deformation comes with a higher energy penalty.

As narrow pores are expected to enhance the energy density, yet the difficulty of penetrating narrow pores might compromise the power density in electric double layer capacitors, it is likely that an optimum pore size exists to enhance the performance of the device. Future research will identify how the optimum pore size depends on the applied voltage, on the electrolyte composition, and also on the functionalization of the pore openings, which might affect the molecular mechanism by which ions enter/exit the pores.

Acknowledgements

Notes and references

1 (a) M. Winter and R. J. Brodd, *Chem. Rev.*, 2004, **104**, 4245–4269; (b) R. Kötz and M. Carlen, *Electrochim. Acta*, 2000, **45**, 2483–2498.

2 B. E. Conway, *Electrochemical supercapacitors: scientific fundamentals and technological applications*, Kluwer Academic/Plenum Publishers, New York, 1999.

3 Y. Oren, *Desalination*, 2008, **228**, 10–29.

4 (a) L. L. Zhang and X. S. Zhao, *Chem. Soc. Rev.*, 2009, **38**, 2520–2531; (b) P. Simon and Y. Gogotsi, *Nat. Mater.*, 2008, **7**, 845–854.

5 A. Lewandowski, A. Olejniczak, M. Galinski and I. Stepniak, *J. Power Sources*, 2010, **195**, 5814–5819.

6 J. Chmiola, G. Yushin, Y. Gogotsi, C. Portet, P. Simon and P. L. Taberna, *Science*, 2006, **313**, 1760–1763.

7 (a) B. Kim, H. Chung and W. Kim, *J. Phys. Chem. C*, 2010, **114**, 15223–15227; (b) D. Yu and L. Dai, *J. Phys. Chem. Lett.*, 2009, **1**, 467–470; (c) C. Largeot, C. Portet, J. Chmiola, P.-L. Taberna, Y. Gogotsi and P. Simon, *J. Am. Chem. Soc.*, 2008, **130**, 2730–2731; (d) A. Izadi-Najafabadi, D. N. Futaba, S. Iijima and K. Hata, *J. Am. Chem. Soc.*, 2010, **132**, 18017–18019.

8 (a) J. Chmiola, C. Largeot, P.-L. Taberna, P. Simon and Y. Gogotsi, *Angew. Chem., Int. Ed.*, 2008, **47**, 3392–3395; (b) J. Huang, B. G. Sumpter and V. Meunier, *Angew. Chem., Int. Ed.*, 2008, **47**, 520–524.

9 (a) G. Feng, R. Qiao, J. Huang, B. G. Sumpter and V. Meunier, *J. Phys. Chem. C*, 2010, **114**, 18012–18016; (b) L. Yang and S. Garde, *J. Chem. Phys.*, 2007, **126**, 084706; (c) Y. Shim and H. J. Kim, *ACS Nano*, 2010, **4**, 2345–2355.

10 (a) R. K. Kalluri, D. Konatham and A. Striolo, *J. Phys. Chem. C*, 2011, **115**, 13786–13795; (b) A. A. Chialvo and P. T. Cummings, *J. Phys. Chem. A*, 2011, **115**, 5918–5927; (c) M. V. Fedorov and A. A. Kornyshev, *Electrochim. Acta*, 2008, **53**, 6835–6840; (d) R. M. Lynden-Bell and J. C. Rasaiah, *J. Chem. Phys.*, 1996, **105**, 9266–9280; (e) Y. W. Tang, K.-Y. Chan and I. Szalai, *J. Phys. Chem. B*, 2004, **108**, 18204–18213.

11 (a) G. Feng, R. Qiao, J. Huang, S. Dai, B. G. Sumpter and V. Meunier, *Phys. Chem. Chem. Phys.*, 2011, **13**, 1152–1161; (b) S. Wang, S. Li, Z. Cao and T. Yan, *J. Phys. Chem. C*, 2009, **114**, 990–995; (c) S. Chen, G. Wu, M. Sha and S. Huang, *J. Am. Chem. Soc.*, 2007, **129**, 2416–2417; (d) S. Chen, K. Kobayashi, Y. Miyata, N. Imazu, T. Saito, R. Kitaura and H. Shinohara, *J. Am. Chem. Soc.*, 2009, **131**, 14850–14856; (e) S. Kondrat, N. Georgi, M. V. Fedorov and A. A. Kornyshev, *Phys. Chem. Chem. Phys.*, 2011, **13**, 11359–11366; (f) J. Vatamanu, O. Borodin and G. D. Smith, *J. Am. Chem. Soc.*, 2010, **132**, 14825–14833; (g) L. Yang, B. H. Fishbine, A. Migliori and L. R. Pratt, *J. Am. Chem. Soc.*, 2009, **131**, 12373–12376; (h) G. Feng and P. T. Cummings, *J. Phys. Chem. Lett.*, 2011, **2**, 2859–2864.

12 (a) S. Porada, L. Weinstein, R. Dash, A. van der Wal, M. Bryjak, Y. Gogotsi and P. M. Biesheuvel, *ACS Appl. Mater. Interfaces*, 2012, **4**, 1194–1199; (b) M. E. Suss, T. F. Baumann, W. L. Bourcier, C. M. Spadaccini, K. A. Rose, J. G. Santiago and M. Stadermann, *Energy Environ. Sci.*, 2012, **5**, 9511–9519.

13 J. Biener, M. Stadermann, M. Suss, M. A. Worsley, M. M. Biener, K. A. Rose and T. F. Baumann, *Energy Environ. Sci.*, 2011, **4**, 656–667.

14 J. Biener, S. Dasgupta, L.-H. Shao, D. Wang, M. A. Worsley, A. Wittstock, J. R. I. Lee, M. M. Biener, C. Orme, S. O. Kucheyev, B. C. Wood, T. M. Willey, A. V. Hamza, J. Weissmüller, H. Hahn and T. F. Baumann, *Adv. Mater.*, 2012, **24**, 5083–5087.

15 M. E. Suss, T. F. Baumann, M. A. Worsley, K. A. Rose, T. F. Jaramillo, M. Stadermann and J. G. Santiago, to be submitted.

16 R. K. Kalluri, J. Biener, M. M. Biener and A. Striolo, to be submitted.

17 J. C. Palmer and K. E. Gubbins, *Microporous Mesoporous Mater.*, 2012, **154**, 24–37.

18 L. X. Dang, *J. Am. Chem. Soc.*, 1995, **117**, 6954–6960.

19 M. Předota, Z. Zhang, P. Fenter, D. J. Wesolowski and P. T. Cummings, *J. Phys. Chem. B*, 2004, **108**, 12061–12072.

20 H. J. C. Berendsen, J. R. Grigera and T. P. Straatsma, *J. Phys. Chem.*, 1987, **91**, 6269–6271.

21 A. Cheng and W. A. Steele, *J. Chem. Phys.*, 1990, **92**, 3858–3866.

22 (a) S. Plimpton, *J. Comput. Phys.*, 1995, **117**, 1–19; (b) http://lammps.sandia.gov.

23 (*a*) W. G. Pell, B. E. Conway and N. Marincic, *J. Electroanal. Chem.*, 2000, **491**, 9–21; (*b*) J. P. Zheng and T. R. Jow, *J. Electrochem. Soc.*, 1997, **144**, 2417–2420.

24 K.-L. Yang, S. Yiacoumi and C. Tsouris, *J. Chem. Phys.*, 2002, **117**, 8499–8507.

25 C.-H. Hou, P. Taboada-Serrano, S. Yiacoumi and C. Tsouris, *J. Chem. Phys.*, 2008, **129**, 224703.

26 D. E. Smith and L. X. Dang, *J. Chem. Phys.*, 1994, **100**, 3757–3766.

27 K.-L. Yang, S. Yiacoumi and C. Tsouris, *J. Electroanal. Chem.*, 2003, **540**, 159–167.

28 K.-L. Yang, T.-Y. Ying, S. Yiacoumi, C. Tsouris and E. S. Vittoratos, *Langmuir*, 2001, **17**, 1961–1969.

29 *CRC Handbook of Chemistry and Physics*, Florida, 2011–2012.

30 Y. Marcus, *Chem. Rev.*, 1988, **88**, 1475–1498.

31 B. Tansel, J. Sager, T. Rector, J. Garland, R. F. Strayer, L. Levine, M. Roberts, M. Hummerick and J. Bauer, *Sep. Purif. Technol.*, 2006, **51**, 40–47.

32 S. E. Rodriguez-Cruz, R. A. Jockusch and E. R. Williams, *J. Am. Chem. Soc.*, 1998, **120**, 5842–5843.

33 M. Mueller and B. Kastening, *J. Electroanal. Chem.*, 1994, **374**, 149–158.

34 Q. Shao, L. Huang, J. Zhou, L. Lu, L. Zhang, X. Lu, S. Jiang, K. E. Gubbins and W. Shen, *Phys. Chem. Chem. Phys.*, 2008, **10**, 1896–1906.

35 A. A. Chialvo, M. S. Gruszkiewicz, J. M. Simonson, D. A. Palmer and D. R. Cole, *J. Solution Chem.*, 2009, **38**, 827–841.